LETTER

doi:10.1038/nature25008

Perovskite nickelates as electric-field sensors in salt water

Zhen Zhang[1]*, Derek Schwanz[1]*, Badri Narayanan[2]†, Michele Kotiuga[3], Joseph A. Dura[4], Mathew Cherukara[2], Hua Zhou[5], John W. Freeland[5], Jiarui Li[6], Ronny Sutarto[7], Feizhou He[7], Chongzhao Wu[8], Jiaxin Zhu[9], Yifei Sun[1], Koushik Ramadoss[1], Stephen S. Nonnenmann[9], Nanfang Yu[8], Riccardo Comin[6], Karin M. Rabe[3], Subramanian K. R. S. Sankaranarayanan[2] & Shriram Ramanathan[1]

Designing materials to function in harsh environments, such as conductive aqueous media, is a problem of broad interest to a range of technologies, including energy, ocean monitoring and biological applications[1–4]. The main challenge is to retain the stability and morphology of the material as it interacts dynamically with the surrounding environment. Materials that respond to mild stimuli through collective phase transitions and amplify signals could open up new avenues for sensing. Here we present the discovery of an electric-field-driven, water-mediated reversible phase change in a perovskite-structured nickelate, $SmNiO_3$[5–7]. This prototypical strongly correlated quantum material is stable in salt water, does not corrode, and allows exchange of protons with the surrounding water at ambient temperature, with the concurrent modification in electrical resistance and optical properties being capable of multimodal readout. Besides operating both as thermistors and pH sensors, devices made of this material can detect sub-volt electric potentials in salt water. We postulate that such devices could be used in oceanic environments for monitoring electrical signals from various maritime vessels and sea creatures.

Pristine $SmNiO_3$ (SNO), a quantum material in the family of strongly correlated electron systems[5,6], is a perovskite-structured rare-earth nickelate[7]. The high ionic conductivity that has been noted in SNO solid-state fuel cells, comparable to that of the best-performing proton conductors, is due in part to their covalent ground state and low-energy phonon modes[8]. Figure 1a illustrates SNO submerged in water in the presence of an electric bias generated by a counter electrode. Under negative electric potentials, protons intercalate into the SNO lattice, accompanied by an uptake of electrons released by oxidation at the counter-electrode. As a result, a saltwater-mediated transition from pristine SNO to hydrogenated SNO (HSNO) occurs under bias. This proton influx accompanies a modification of the electronic configuration of the Ni 3*d* orbitals, unlike in electrochromic oxides such as WO_3, where transition to a metallic state occurs upon cation doping (Supplementary Information section 1). The doping-driven resistance change for the uptake of one electron per formula unit is about 10,000 times larger for SNO than for WO_3. As Fig. 1b, c shows, the partially filled e_g orbital with small transport gap for charge carriers in SNO becomes half-filled in HSNO, where strong Mott–Hubbard electron–electron interaction arises and localizes the charge carriers.

To demonstrate the response of the perovskite devices when encountering an electric bias in salt water, SNO thin films were incorporated into a three-terminal electrochemical cell and served as working electrodes. An electric potential was applied across the aqueous solution using a graphite counter-electrode referenced to a standard Ag/AgCl reference electrode. Because water is generally a harsh environment for oxides[9] and the formation of hydroxides can be accompanied by massive crystal structure changes (for example, in hydrated cobaltites[10]), the stability of SNO in aqueous solution was first investigated without electric potentials. Figure 1d compares the temperature-dependent electrical resistivity of pristine SNO with that of a SNO thin film submerged for 24 h in a 0.6 M NaCl solution at room temperature. Nearly identical resistivity–temperature curves are observed in both samples, indicating stability. The expected thermally induced insulator–metal transition in submerged SNO at about 130 °C is still present, which is often used as an indicator of film quality (Extended Data Fig. 1a). SNO is robust in both weakly acidic (0.01 M citric acid, pH = 2.7) and basic (0.01 M KOH, pH = 12) solutions (Extended Data Fig. 1b) over 180 min. This stability of SNO in aqueous environments over a range of pH values enables us to study its response to electric bias in a systematic manner (Supplementary Information section 2). Moreover, the open-circuit potential of SNO relative to the standard Ag/AgCl electrode varies with the pH value of the aqueous solutions; this feature of SNO, together with its temperature-dependent electrical resistivity, enable it to operate as a local environmental sensor (Extended Data Fig. 2a, b).

Figure 1e shows the electrical resistivity of SNO after applying negative electric potential up to −4.0 V (versus the Ag/AgCl electrode) in a 0.6 M NaCl solution, the salinity of which is similar to that of sea water. Upon application of negative electric potential, the electrical resistivity of SNO exhibits an increase by more than five orders of magnitude along with a noticeable colour change (Fig. 1e). The resistivity of water-treated SNO (Fig. 1d, red curve) decreases smoothly with increasing temperature, indicating an insulating state with localized electrons. The substantial change of the electrical properties of water-treated SNO is non-volatile at ambient conditions (Extended Data Fig. 1c), indicating that it is not a simple electrostatic field effect induced by charge accumulation at the surface, but a water-mediated phase transition. The observed phase change occurs regardless of the aqueous solution (examples include 0.01 M KOH, 0.6 M NaCl and 0.01 M citric acid) and substrate (for example, $LaAlO_3$ (001) and Si (100)) used. A cross-sectional conducting atomic force microscopy (conducting AFM) image of SNO, which was acquired after the film was used for sensing an electric potential in aqueous solution (Fig. 1f, topography), shows that no corrosion occurs beneath the SNO–water interface and the thin film retains structural integrity. The cross-sectional conducting AFM image of the current reveals that the insulating phase (black

[1]School of Materials Engineering, Purdue University, West Lafayette, Indiana 47907, USA. [2]Center for Nanoscale Materials, Argonne National Laboratory, Argonne, Illinois 60439, USA. [3]Department of Physics and Astronomy, Rutgers University, Piscataway, New Jersey 08854, USA. [4]NIST Center for Neutron Research, National Institute of Standards and Technology, Gaithersburg, Maryland 20899, USA. [5]X-ray Science Division, Advanced Photon Source, Argonne National Laboratory, Argonne, Illinois 60439, USA. [6]Department of Physics, Massachusetts Institute of Technology, Cambridge, Massachusetts 02139, USA. [7]Canadian Light Source, University of Saskatchewan, Saskatoon, Saskatchewan S7N 2V3, Canada. [8]Department of Applied Physics and Applied Mathematics, Columbia University, New York 10027, USA. [9]Department of Mechanical and Industrial Engineering, University of Massachusetts – Amherst, Amherst, Massachusetts 01003, USA.
†Present address: Materials Science Division, Argonne National Laboratory, Lemont, Illinois 60439, USA.
*These authors contributed equally to this work.

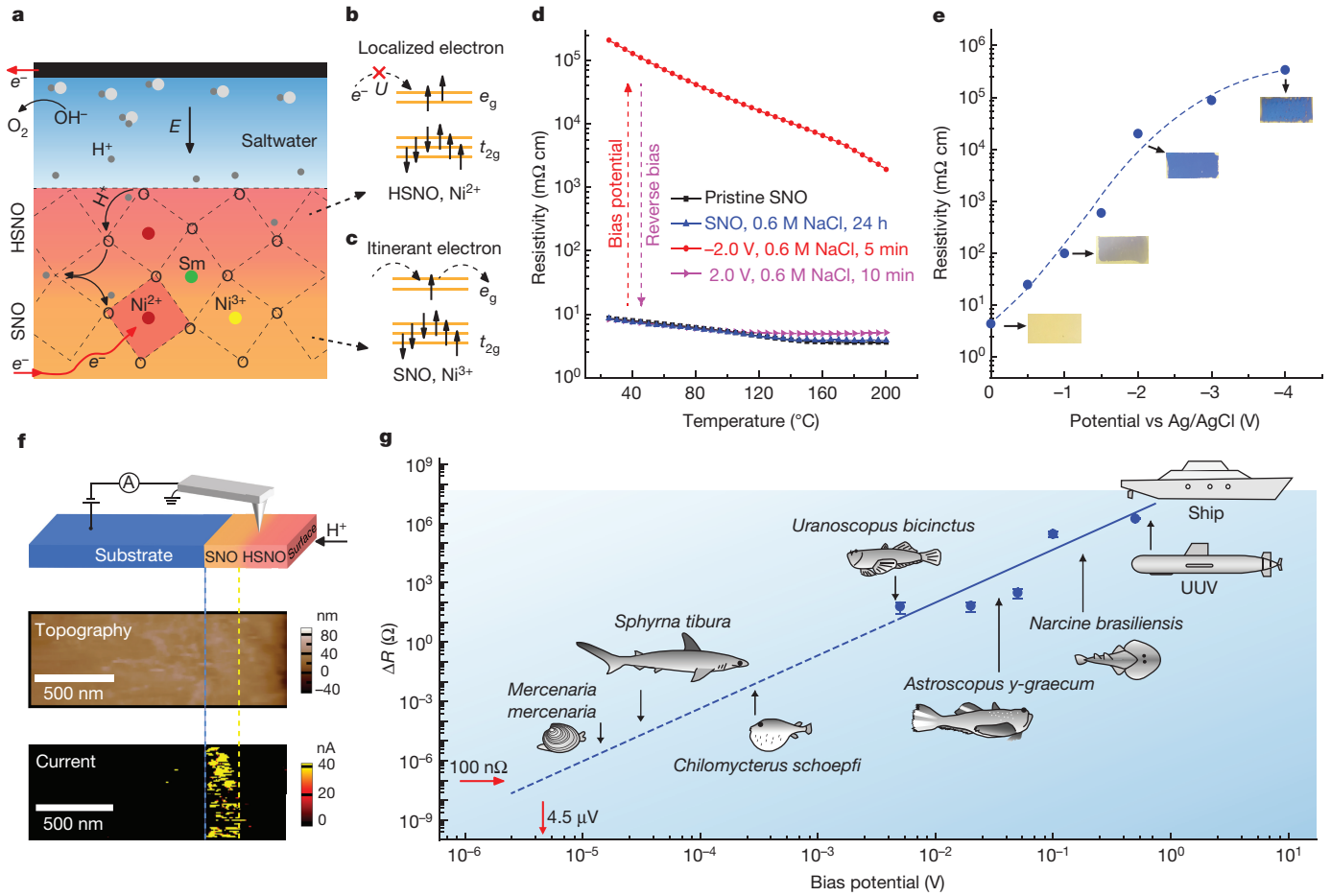

Figure 1 | Saltwater-submersible nickelate sensors. **a**, Illustration of the saltwater-mediated phase transition in SNO. Under bias, the protons intercalate and diffuse into the SNO lattice accompanied by electron transfer from the counter-electrode (*E*, electric field). **b**, **c**, Schematics of the electronic structure of Ni 3*d* orbitals in hydrogenated (**b**) and pristine (**c**) SNO. The electrons become localized in HSNO owing to the strong Coulomb repulsion in doubly occupied e_g orbitals above the t_{2g} orbitals. *U* represents the on-site electron–electron correlation. **d**, After being submerged in a 0.6 M NaCl solution for 24 h at room temperature, the electrical resistivity of SNO is similar to that of pristine SNO, indicating its robustness in water. The red curve shows increased electrical resistivity after applying a negative bias of −2.0 V in a 0.6 M NaCl solution for 5 min. The sample is then treated under a reverse bias of 2.0 V for 10 min, and its electrical resistivity curve (purple) is almost recovered to its original state. **e**, Electrical resistivity and colour change of SNO thin films after applying various bias potentials in a 0.6 M NaCl solution for 10 s. **f**, Cross-sectional conducting AFM images of SNO after bias treatment, showing reduced current owing to the phase change. **g**, The experimentally observed change in the electrical resistance (ΔR) for bias potentials from 0.5 V to 5 mV (Extended Data Fig. 2c). This measurement range spans all maritime vessels and several marine animals, as marked. The resistance change beyond the present measurement window (<5 mV) is estimated by linear extrapolation. With high-resolution resistance measurements (100 nΩ; see Methods), the SNO device would be sensitive down to about 4.5 μV, extending to even smaller marine animals[11–16]. Error bars show standard deviations. UUV, unmanned underwater vehicle.

colour, HSNO) propagates into the SNO thin film from the water interface, indicating the intercalation and diffusion of protons into SNO during sensing. Additional conducting AFM images taken in-plane (Extended Data Fig. 3 and Supplementary Information section 3) further rule out corrosion or morphological degradation during water treatment as the origin of the resistance change and demonstrate the uniformity and diffusional nature of the water-mediated phase transition in SNO.

The water-treated thin films can be brought back to the low-resistivity state by the application of a reverse bias (Fig. 1d and Extended Data Fig. 1a, purple curve), indicating their capability to detect local fluctuations of an electric potential in water. We find that the electrical resistivity of SNO can change consistently following the application of a bias potential ranging from ±0.5 V to ±0.005 V over multiple cycles (Extended Data Fig. 2c). Figure 1g shows the modulation of the electrical resistance of SNO when a bias potential down to the level of millivolts is applied to evaluate the measurement sensitivity of SNO. The sensitivity of our SNO device can be extrapolated to show a microvolt-level detection ability in oceans, which is enabled by high-resolution resistance measurements (see Methods) in the entire range of bioelectric potentials generated by numerous marine species up to galvanic potentials from ships and unmanned underwater vehicles[11–16].

The sensing mechanism of SNO is analogous to the electroreception organs of elasmobranch species such as sharks, rays and skates: the ampullae of Lorenzini[17–19]. These ampullae are located around the mouths of sharks[20]; the distinctive structure of a single ampulla is shown schematically in Extended Data Fig. 2d. The jelly inside the ampulla, which has excellent proton conductivity[21] and enables thermal sensing[22], conducts ions from the nearby sea water to the membrane located at the bottom of the ampulla. The membrane contains sensing cells that react to an electric potential applied across them (Extended Data Fig. 2d). Under electric bias, ionic channels on the apical side of the sensing cells open and allow a flux of charged ions, which causes the sensing cell to release neurotransmitters to synapses at the bottom, informing the brain[17,20]. Thus, the ampullae of Lorenzini enable these sharks to detect bioelectric fields emitted by prey fish[18]. This suggests an analogy between the nickelate sensor and the electroreception organ of sharks. We calculated the detection distance of SNO and found a similar length scale to what has been reported for the elasmobranch electroreceptors (Extended Data Fig. 2e). Furthermore, the response

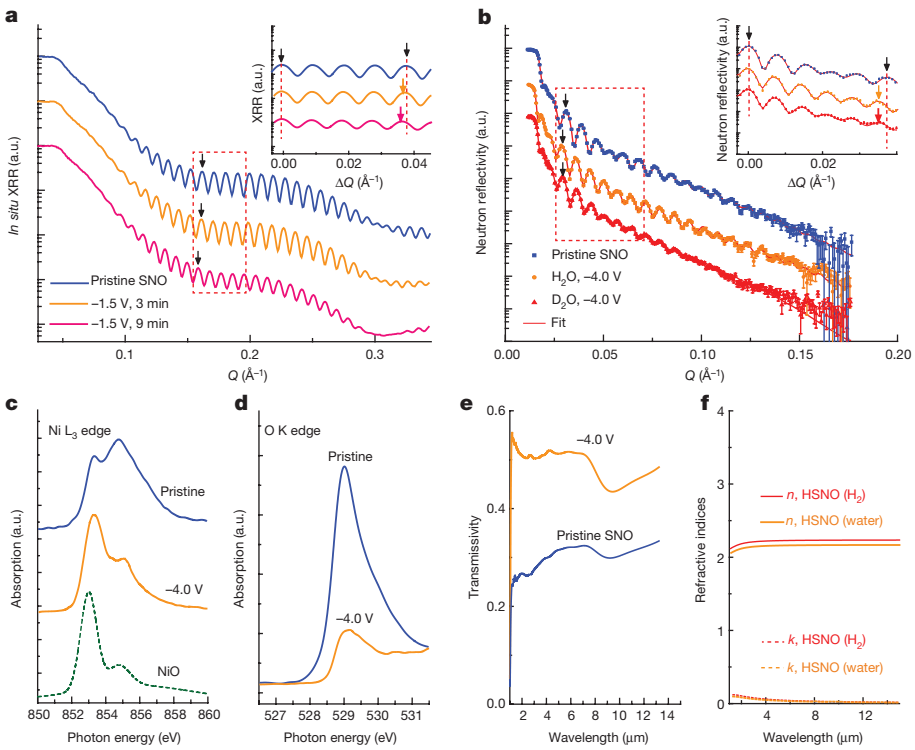

Figure 2 | Mechanism of electric-field sensing in perovskite nickelate. a, Comparison of *in situ* synchrotron XRR curves for pristine and water-treated SNO thin films after applying bias for 3 min and 9 min successively. The inset shows a magnified area of the XRR curves normalized to the oscillation peak for a scattering vector $Q \approx 0.16\ Å^{-1}$ (a.u., arbitrary units). **b**, Neutron reflectometry data, error bars and associated fits for pristine, hydrogenated and deuterated SNO thin films. Error bars represent one standard error. The inset shows a magnified area comparing oscillations normalized to the peak at $Q \approx 0.03\ Å^{-1}$. **c**, X-ray absorption curves of the Ni L_3 edge of pristine and water-treated SNO, compared with that[25] of NiO. **d**, X-ray absorption curves of the O K edge of pristine and water-treated SNO. **e**, Optical transmission spectra of water-treated SNO, showing 100% increased transmissivity in the near-infrared. **f**, Comparison of the real (n) and imaginary (k) parts of the refractive indices of water-treated SNO and dry H_2-gas-treated SNO[27].

time of our SNO devices is in the same range as that of the elasmobranch electroreceptors (Extended Data Fig. 2f).

Charge transfer was observed during the water-mediated phase transition of SNO, as expected. A cathodic current peak (Extended Data Fig. 4a, b) appears in cyclic voltammograms of SNO at negative potentials, indicating the occurrence of a reduction reaction. The magnitude of the electric potential needed to trigger the reduction reaction of SNO increases with increasing pH value (Extended Data Fig. 4a), indicating the close relationship between water-mediated conductance modulation and the activity of protons in aqueous solutions. Fitting of the scan rate dependence of the cathodic current peak with the Randles–Sevcik equation[23] indicates that Ni^{3+} in SNO is almost fully reduced to Ni^{2+} after the reaction (Extended Data Fig. 4c and Supplementary Information section 4).

To investigate the microscopic mechanism of environmental sensing, *in situ* synchrotron X-ray reflectivity (XRR) measurements (Extended Data Fig. 5) were performed on SNO submerged in a 0.01 M KOH/water solution. Upon applying a bias potential of −1.5 V (Fig. 2a), the XRR results show a noticeable decrease in their oscillation period with increasing duration of the applied potential (Fig. 2a inset), indicating a substantial expansion of film thickness[24]. Synchrotron XRR investigations (Extended Data Fig. 6) show that such expansion occurs regardless of the solution type and is attributed to the increased lattice constant of SNO after the treatment.

Although it is extremely challenging to detect protons directly in solids, neutron scattering is among the best available techniques and is also sensitive to hydrogen isotopes. Neutron reflectivity curves for SNO are shown in Fig. 2b for the pristine film and films treated in D_2O (deuterated 'heavy' water) and H_2O solutions. The decrease in the oscillation period of the neutron reflectivity curves after H_2O or D_2O treatment (Fig. 2b inset) corresponds to a film expansion of about 6.9% and a decrease in film density (Supplementary Information section 5). The fitted neutron scattering length density profiles (Extended Data Fig. 7) show a considerable increase in the SNO region when H_2O is replaced with D_2O. This is consistent with the larger neutron scattering cross-section of D^+ relative to H^+. The isotopic substitution results therefore show clearly the intercalation and transport of H^+ (or D^+) from the solution to SNO, which is similar to the ion transfer observed in the membranes of ampullae of Lorenzini.

Synchrotron X-ray absorption spectroscopy (XAS) measurements were carried out near the Ni L_3 edge and the O K edge of water-treated SNO. As Fig. 2c shows, with proton intercalation, the Ni L_3-edge absorption peak shifts its weight from 855 eV to 853 eV, similarly to the absorption edge seen[25] in NiO, indicating that Ni exhibits divalency after water treatment. Because the covalent nature of the Ni–O bond in SNO, where the electronic configuration of the ground state is dominated by the $3d^8\underline{L}$ state (where $\underline{L}$ denotes the existence of a ligand hole in the O $2p$ orbital)[25,26], we further studied the evolution of the O K edge after the water treatment. As Fig. 2d shows, suppression of the O K-edge absorption peak at 529 eV occurs after the treatment, indicating a reduced oxygen-projected density of unoccupied states caused by doping-induced band filling. Therefore, the XAS results of both the Ni L_3 edge and the O K edge demonstrate the formation of Ni^{2+} with the $3d^8$ configuration, resulting from charge transfer associated with proton intercalation after the water treatment. The charge transfer noted here is expected from the cyclic voltammetry observations.

Optical spectra of water-treated SNO were measured for further comparison with gas-phase proton-doped samples (that is, samples never exposed to water). As Fig. 2e shows, the transmissivity of water-treated SNO in the near- and mid-infrared frequency range increases compared to that of pristine SNO. As a result, SNO becomes more transparent in the infrared and visible wavelengths (Extended Data Fig. 8d). The reflectivity and absorptivity (Extended Data Fig. 8a, b) decrease concomitantly in water-treated SNO owing to the localization of charge carriers and opening of the optical bandgap. The real and imaginary parts (n and k, respectively) of the refractive index of water-treated SNO (Fig. 2f), which were calculated using transfer matrix formalism (Supplementary Information section 6), are in good agreement with those of HSNO treated with dry H_2 gas, without exposure to water[27]. This conclusion is further supported by finite-difference time-domain simulations of the optical spectra of water-treated SNO (Extended Data Fig. 8c). These results prove that the primary mechanism of sensing is proton intercalation into the SNO lattice, and not corrosion or degradation of the perovskite. The overall reaction taking place in SNO during electric potential sensing in an

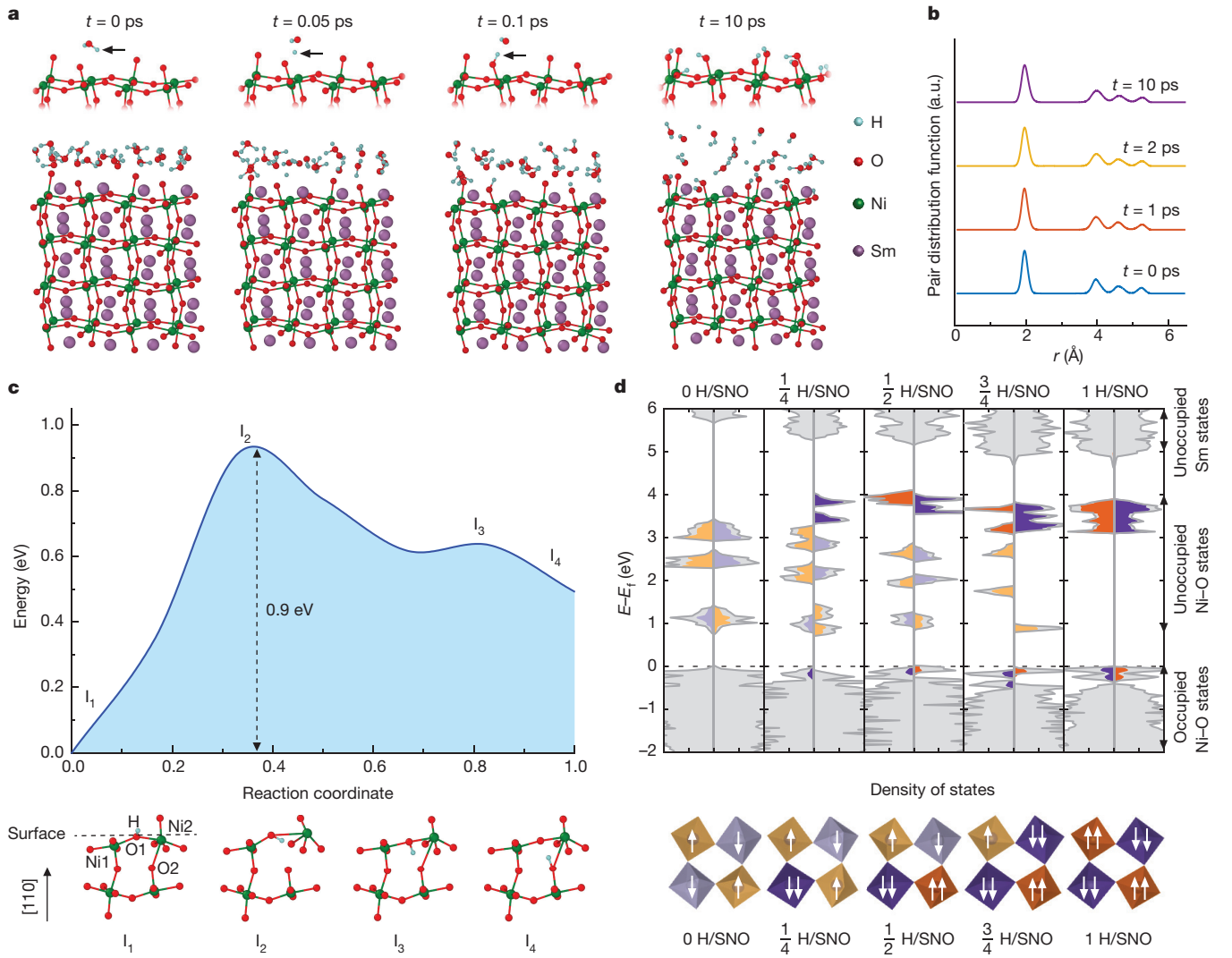

Figure 3 | First-principles calculations of SNO–water interaction and HSNO. a, AIMD simulations of water-mediated protonation of a SNO surface at 300 K. The top images show the evolution of a representative water molecule and the NiO_6 octahedra in the SNO layer closest to water. **b**, Surface stability of SNO, characterized by the Ni–O pair distribution function as a function of the separation distance r at various time intervals. **c**, Energy landscape and atomic-scale pathway of intercalation of surface protons into the SNO lattice. The potential energy is shown along the most preferred migration pathway, together with selected configurations along this pathway (labelled as I_1–I_4). **d**, First-principles calculation of hydrogen-intercalated SNO. The top panel shows the total density of states (grey) as a function of the difference between the energy (E) and the Fermi energy (E_f), with 0–1 added H atoms per SNO formula unit. The unoccupied projected density of states on each Ni site and the Ni projected density of states associated with localized electrons are shown in orange and purple, respectively, corresponding to inequivalent Ni sites. The lower panel shows a schematic of the occupied Ni e_g levels for each scenario. The darker hues indicate Ni sites with two occupied e_g states and the colours correspond to those in the upper panel.

aqueous environment is therefore $H^+_{aqueous} + SNO_{solid} + e^- \leftrightarrow HSNO_{solid}$, where the valence of Ni ions is reduced from Ni(III) in SNO to Ni(II) in HSNO.

Ab initio molecular dynamics (AIMD) simulations were carried out to study the underlying atomic-scale mechanisms of the water-mediated phase transition in SNO. As Fig. 3a shows, the water proximal to the SNO surface dissociates into a free proton and OH^-. The proton migrates to the oxide/water interface and binds to a surface oxygen atom (Supplementary Video 1). We find an increased uptake of protons by the surface oxygen atoms of SNO, which has little impact on the structural integrity of the oxide interface (Fig. 3a, $t = 10$ ps). The protonation of the SNO surface and its structural stability in water are also observed at elevated temperature (500 K; Extended Data Fig. 9a, b and Supplementary Video 2) and with either excess OH^- radicals or excess protons. Besides primary surface events, such as proton migration and binding, the AIMD trajectories reveal that the OH^- (arising from water dissociation) can bind to the under-coordinated Ni atoms (fewer than six O nearest neighbours) on the surface and restore the NiO_6 octahedra (Fig. 3a, $t = 10$ ps), which further improves the surface stability. The Ni–O pair distribution functions (Fig. 3b and Extended Data Fig. 9c) remain sharp and well defined. The peaks in the pair distribution functions can be resolved even at long distances (above 5 Å), indicating that the long-range structural order in SNO is preserved. The stability of the SNO surface stems in part from the high vacancy formation energies in pristine SNO; for example, the oxygen vacancy formation energy in SNO, as obtained from our density functional theory (DFT) calculations, is 2.95 eV, more than three times higher than the energy barrier for proton intercalation (0.9 eV in Fig. 3c).

Nudged elastic band calculations in the framework of DFT were performed to estimate the energy landscape and to identify the energetically preferred pathways for H^+ intercalation into SNO (Fig. 3c). Initially, the proton is bound to a surface oxygen atom O1 (image I_1 in Fig. 3c) at a distance of about 3.7 Å from atom O2, where atom O1 is the shared corner of two NiO_6 octahedra centred at nickel atoms Ni1

and Ni2. The Ni1–O1–Ni2 bond angle is about 145° and the length of the Ni2–O2 bond is approximately 2.5 Å, similar to that of bulk SNO. The proton first rotates about O1 while being bound to it, so that it enters the sub-surface layer of the SNO slab and reduces the O2–H distance to about 2.6 Å (image I_2 in Fig. 3c). This rotation of the O1–H bond distorts the surface layer considerably, which manifests itself in an increased Ni2–O2 distance of about 3.43 Å and a substantial change of the Ni1–O1–Ni2 angle (about 153°). This surface distortion process is associated with a barrier of about 0.9 eV. Further rotation of the O1–H bond brings the proton close to O2 (O2–H distance of approximately 1.5 Å; image I_3 in Fig. 3c) while increasing the inter-octahedral angle Ni1–O1–Ni2 to about 175°, and leads to the concurrent healing of the Ni2–O2 bond (image I_4 in Fig. 3c), which thus preserves the SNO framework upon intake of protons. Once the proton is intercalated into the SNO lattice, intra-octahedral proton hopping occurs even at room temperature, as seen in the *ab initio* simulations (Supplementary Video 3), indicating facile proton diffusion within SNO. The calculated energy barrier associated with the migration of protons within the SNO lattice is about 0.27 eV, which is low compared to those of other proton-conducting oxides[28] (0.4–0.6 eV). Volume expansion is observed in simulations after proton intercalation (Extended Data Fig. 10a–g and Supplementary Information section 7), which is in agreement with reflectometry measurements.

Density functional theory calculations (Fig. 3d) show that as each hydrogen atom is added to the supercell, its electron is transferred to a previously unoccupied Ni–O orbital of pristine SNO. The transfer of the electron can also be seen in the difference between the charge density of the combined HSNO system and that of the sum of SNO and H, which shows charge depletion around the H and a corresponding charge accumulation around the adjacent Ni and O (Extended Data Fig. 10h, i). Owing to electron–electron correlations, this state is shifted down into the valence band, while the remaining unoccupied states of that Ni are shifted up in energy. The bandgap remains almost unchanged until an electron has been added to each Ni atom. Both of these observations are consistent with the experimentally observed changes in X-ray absorption spectra and the increase in the electrical resistance of SNO that enables effective sensing.

Online Content Methods, along with any additional Extended Data display items and Source Data, are available in the online version of the paper; references unique to these sections appear only in the online paper.

Received 2 May; accepted 31 October 2017.
Published online 18 December 2017.

1. Chen, Y. W. *et al.* Atomic layer-deposited tunnel oxide stabilizes silicon photoanodes for water oxidation. *Nat. Mater.* **10,** 539–544 (2011).
2. Uhlig, H. H. in *Uhlig's Corrosion Handbook* 3rd edn (ed. Revie, R. W.) Ch. 51 (John Wiley & Sons, 2011).
3. Yuh, J. Design and control of autonomous underwater robots: a survey. *Auton. Robots* **8,** 7–24 (2000).
4. Robison, B. H. Deep pelagic biology. *J. Exp. Mar. Biol. Ecol.* **300,** 253–272 (2004).
5. Medarde, M. L. Structural, magnetic and electronic properties of $RNiO_3$ perovskites (R= rare earth). *J. Phys. Condens. Matter* **9,** 1679–1707 (1997).
6. Middey, S. *et al.* Physics of ultrathin films and heterostructures of rare-earth nickelates. *Annu. Rev. Mater. Res.* **46,** 305–334 (2016).
7. Catalan, G. Progress in perovskite nickelate research. *Phase Transit.* **81,** 729–749 (2008).
8. Zhou, Y. *et al.* Strongly correlated perovskite fuel cells. *Nature* **534,** 231–234 (2016).
9. Kritzer, P. Corrosion in high-temperature and supercritical water and aqueous solutions: a review. *J. Supercrit. Fluids* **29,** 1–29 (2004).
10. Pelloquin, D., Barrier, N., Maignan, A. & Caignaert, V. Reactivity in air of the $Sr_3Co_2O_{7-\delta}$ RP= 2 phase: formation of the hydrated $Sr_3Co_2O_5(OH)_2{\cdot}xH_2O$ cobaltite. *Solid State Sci.* **7,** 853–860 (2005).
11. Bedore, C. N. & Kajiura, S. M. Bioelectric fields of marine organisms: voltage and frequency contributions to detectability by electroreceptive predators. *Physiol. Biochem. Zool.* **86,** 298–311 (2013).
12. Baron, V. D. Electric discharges of two species of stargazers from the South China Sea (Uranoscopidae, Perciformes). *J. Ichthyol.* **49,** 1065–1072 (2009).
13. Hirota, M. A method to measure ship's underwater electric field from deck. In *Proc. 2000 Int. Symp. on 'Underwater Technology'* 224–228 (IEEE, 2000); http://ieeexplore.ieee.org/document/852547/.
14. Kim, J.-G., Joo, J.-H. & Koo, S.-J. Development of high-driving potential and high-efficiency Mg-based sacrificial anodes for cathodic protection. *J. Mater. Sci. Lett.* **19,** 477–479 (2000).
15. Bennett, M. V. L., Wurzel, M. & Grundfest, H. The electrophysiology of electric organs of marine electric fishes. *J. Gen. Physiol.* **44,** 757–804 (1961).
16. Mathewson, R., Mauro, A., Amatniek, E. & Grundfest, H. Morphology of main and accessory electric organs of *Narcine brasiliensis* (Olfers) and some correlations with their electrophysiological properties. *Biol. Bull.* **115,** 126–135 (1958).
17. Kalmijn, A. J. The electric sense of sharks and rays. *J. Exp. Biol.* **55,** 371–383 (1971).
18. Kalmijn, A. J. Electric and magnetic field detection in elasmobranch fishes. *Science* **218,** 916–918 (1982).
19. Bellono, N. W., Leitch, D. B. & Julius, D. Molecular basis of ancestral vertebrate electroreception. *Nature* **543,** 391–396 (2017).
20. Fields, R. D. The shark's electric sense. *Sci. Am.* **297,** 74–81 (2007).
21. Josberger, E. E. *et al.* Proton conductivity in ampullae of Lorenzini jelly. *Sci. Adv.* **2,** e1600112 (2016).
22. Brown, B. R. Sensing temperature without ion channels. *Nature* **421,** 495 (2003).
23. Bard, A. J., Faulkner, L. R., Leddy, J. & Zoski, C. G. *Electrochemical Methods: Fundamentals and Applications* 1st edn, Vol. 2 (Wiley, 1980).
24. Daillant, J. & Gibaud, A. (eds) *X-ray and Neutron Reflectivity: Principles and Applications* Vol. 770 (Springer, 2008).
25. Medarde, M. *et al.* $RNiO_3$ perovskites (R= Pr, Nd): nickel valence and the metal-insulator transition investigated by x-ray-absorption spectroscopy. *Phys. Rev. B* **46,** 14975–14984 (1992).
26. Mizokawa, T. *et al.* Electronic structure of $PrNiO_3$ studied by photoemission and x-ray-absorption spectroscopy: band gap and orbital ordering. *Phys. Rev. B* **52,** 13865–13873 (1995).
27. Li, Z. *et al.* Correlated perovskites as a new platform for super-broadband-tunable photonics. *Adv. Mater.* **28,** 9117–9125 (2016).
28. Kreuer, K. D. Proton-conducting oxides. *Annu. Rev. Mater. Res.* **33,** 333–359 (2003).

Supplementary Information is available in the online version of the paper.

Acknowledgements S.R. thanks K. Catania (Vanderbilt University) for discussions on bioelectric fields in marine organisms and B. Robinson and K. Benoit-Bird of the Monterey Bay Aquarium Research Institute for technical discussions on electroreception in sharks. We acknowledge financial support from the Army Research Office (W911NF-16-1-0289, W911NF-16-1-0042), National Science Foundation (DMR-1609898, DMR-1610215), Defense Advanced Research Projects Agency (grant D15AP00111), Office of Naval Research (grants N00014-16-1-2442 and N00014-12-1040) and Air Force Office of Scientific Research (grants FA9550-16-1-0159 and FA9550-14-1-0389). Use of the Center for Nanoscale Materials, an Office of Science user facility, was supported by the US Department of Energy (DOE), the Office of Science, Office of Basic Energy Sciences under contract number DE-AC02-06CH11357. This research used resources of the Advanced Photon Source, a US DOE Office of Science User Facility operated by Argonne National Laboratory under contract number DE-AC02-06CH11357. This research used resources of the National Energy Research Scientific Computing Center, which is supported by the Office of Science of the US DOE under contract number DE-AC02-05CH11231. An award of computer time was provided by the Innovative and Novel Computational Impact on Theory and Experiment (INCITE) programme. This research used resources of the Argonne Leadership Computing Facility at Argonne National Laboratory, which is supported by the Office of Science of the US DOE under contract DE-AC02-06CH11357. S.S.N. acknowledges support from the University of Massachusetts-Amherst through start-up funding. Part of the research described in this paper was performed at the Canadian Light Source, which is supported by the Canada Foundation for Innovation, Natural Sciences and Engineering Research Council of Canada, the University of Saskatchewan, the Government of Saskatchewan, Western Economic Diversification Canada, the National Research Council Canada and the Canadian Institutes of Health Research.

Author Contributions Z.Z., D.S. and S.R. conceived the study. Z.Z. and D.S. fabricated the SNO thin-film devices and performed the electrical, stability, sensing and electrochemical experiments. B.N., M.C. and S.K.R.S.S. performed the AIMD simulations and the nudged elastic band calculations to compute activation barriers. M.K. and K.M.R. performed first-principles electronic structure calculations. D.S. and J.A.D. performed neutron reflectivity measurements. Y.S., D.S. and H.Z. performed X-ray diffraction and X-ray reflectivity measurements. J.W.F., J.L., R.S., F.H. and R.C. performed X-ray absorption measurements. C.W. and N.Y. performed optical measurements and analysis. J.Z. and S.S.N. performed cross-sectional conducting AFM studies. K.R. and Z.Z. performed in-plane conducting AFM studies. Z.Z., D.S., B.N., S.K.R.S.S. and S.R. wrote the manuscript. All authors discussed the results and commented on the manuscript.

Author Information Reprints and permissions information is available at www.nature.com/reprints. The authors declare no competing financial interests. Readers are welcome to comment on the online version of the paper. Publisher's note: Springer Nature remains neutral with regard to jurisdictional claims in published maps and institutional affiliations. Correspondence and requests for materials should be addressed to S.R. (shriram@purdue.edu).

Reviewer Information *Nature* thanks M. Lyons and the other anonymous reviewer(s) for their contribution to the peer review of this work.

METHODS

Synthesis of $SmNiO_3$ thin films. $SmNiO_3$ (SNO) was synthesized by physical vapour deposition and subsequent ultrahigh-pressure annealing in pure oxygen. Substrates were cleaned with acetone and isopropanol, followed by compressed Ar drying. SNO thin films were deposited on the substrates by magnetron co-sputtering of Sm and Ni targets at room temperature in an Ar/O_2 mixture at 0.67 Pa. To obtain the appropriate stoichiometric ratio, Sm was deposited at 160 W (radiofrequency sputtering) and Ni at 80 W (direct-current sputtering). The stoichiometric ratio of Sm and Ni was analysed using energy-dispersive X-ray spectroscopy. The substrates were rotated during deposition to ensure composition homogeneity. The deposited samples were then annealed for 24 h at 500 °C under high-pressure O_2 (10^7 Pa) in a home-built vessel to form the perovskite phase. Both epitaxial and polycrystalline SNO thin films were used in this work to demonstrate the generality of the water-mediated phase transition in SNO. Epitaxial SNO thin films were obtained on single-crystalline $LaAlO_3$ (001) substrates, while polycrystalline SNO thin films were grown on Si (100) wafers.

Aqueous solution preparation. To mimic the salinity of seawater, a 0.6 M NaCl aqueous solution was prepared by dissolving reagent-grade NaCl into micropure (18.2 MΩ cm) water, which has electrical conductivity comparable to that of seawater (5 S m^{-1}). Experiments were performed at ambient temperature, unless otherwise noted. Additional aqueous solutions with a much wider pH range than seawater were studied, including standard buffers (pH = 4.0, 7.0, 10.0), a weakly acidic solution containing no salt (pH = 2.7, 0.01 M citric acid in H_2O), and a weakly basic solution (pH = 12.0, 0.01 M KOH in H_2O) (Supplementary Information section 2). These aqueous environments were designed to cover the wide ranges of temperature and pH found across Earth's oceans.

Sensing experiments in water environments. SNO thin films were incorporated into a three-terminal electrochemical cell. Platinum wire was bonded on the thin films with silver paste, and polyethylene masks (Gamry) were used to expose selected areas of SNO. The SNO film was then submerged into aqueous solutions and connected as a working electrode. The counter-electrode was a graphite rod with large surface area. A Ag/AgCl (saturated KCl) reference electrode was used to control and modulate the electric potential applied. A static electric potential was applied to SNO by a potentiostat. Cyclic voltammetry was performed on SNO samples with identical three-terminal configuration. The sensing and electrochemical tests were performed with a Solartron 1260A electrochemical analyser.

Electrical measurements. After the water-based treatment, the SNO samples were removed from the aqueous solution, rinsed with deionized water, and dried with argon gas. Contact electrodes (Pt) were patterned on the treated area. The SNO thin films were then transferred to a controlled-temperature probe station and their electrical resistance was measured with a Keithley 2635A source meter.

An ohmmeter with sensitivity of 100 nΩ is commercially available. Higher sensitivity can be obtained by utilizing a lock-in amplifier in the amplitude- or phase-sensitive mode, which is routinely used in low-temperature physics research.

Conducting AFM measurements. To observe the propagation of the HSNO phase after sensing electric potential in water, cross-sectional conducting AFM measurements were carried out on SNO films (about 500 nm thickness) grown on Si (100) substrates. The SNO was treated at a bias potential of −2.0 V (versus Ag/AgCl) for 30 min in a 0.6 M NaCl aqueous solution. After the treatment, the sample was vertically mounted in epoxy resin. The cross-sectional surface subsequently underwent multiple mechanical polishing steps, with the final polish using a 1-μm-diameter diamond suspension. The opposite cross-sectional surface was coated with silver paste to form the bottom electrode. The conducting AFM cross-sectional imaging was performed through a Pt/Ir-coated tip (Arrow-CONTPt, Nanoworld; force constant 0.2 N m^{-1}) connected to a dual-gain transimpedance amplifier (ORCA) in a commercial system (Oxford Instruments/Asylum Research Cypher ES). Topographic and current images were collected simultaneously with a bias of 5.0 V applied to the bottom Ag electrode, a setpoint of 0.06 V and a scanning rate of 1 Hz. Additional conducting AFM measurements of the top surface of a water-treated SNO sample were conducted with an Asylum MFP3D stand-alone atomic force microscope using Asylum ASYELEC-01 conductive tips (Si coated with Ti/Ir). The AFM tip was grounded and a bias of 1.0 V was applied to the sample surface. A resistor of 1 MΩ was connected in series to the SNO sample to limit the current and protect the conducting AFM tips. The current was amplified using current amplifiers (dual-gain, ORCA) with a sensitivity of 1 V μA^{-1} and 1 V nA^{-1}. The scanning rate was 1 Hz. For the top-surface conducting AFM measurement, a SNO thin film (70 nm) was grown on a Si (100) substrate. A selected area of the sample was treated at a bias potential of −4.0 V (versus Ag/AgCl) in a 0.6 M NaCl aqueous solution for 10 s.

X-ray reflection and diffraction measurements. Synchrotron XRR and X-ray diffraction measurements of the SNO samples were carried out on a five-circle diffractometer with χ-circle geometry (in which the sample can be rotated around the centre of the diffractometer), using an X-ray energy of 20 keV (wavelength $\lambda = 0.6197$ Å) at beamline 12-ID-D of the Advanced Photon Source of Argonne National Laboratory. The X-ray beam had a total flux of 4.0×10^{12} photons s^{-1} and was vertically focused by beryllium-compound refractive lenses to a beam profile below 50 μm. Scans along the Q_z and L directions of the HKL reciprocal space were obtained by subtracting the diffuse background contributions using the two-dimensional images acquired with a two-dimensional pixel array detector (Dectris PILATUS 100K, with a 1-mm-thick Si sensor chip and 10^5 pixels). Additional X-ray diffraction measurements over a wide range of scattering angles were carried out using the PANalytical MRD X'Pert Pro diffractometer with Cu Kα X-rays (wavelength $\lambda = 1.5418$ Å). For *in situ* XRR measurements, epitaxial SNO samples with thicknesses of 70 nm were grown on a $LaAlO_3$ (001) substrate. Each sample was attached to an electrochemical cell (Extended Data Fig. 5) filled with a 0.01 M KOH aqueous solution. The XRR data of SNO were measured *in situ* after applying a bias potential of −1.5 V (versus Ag/AgCl) for 3 min and 9 min. Additional *ex situ* XRR measurements of SNO in various aqueous solutions were carried out. The samples were treated separately in aqueous solutions of 0.01 M citric acid and 0.01 M KOH by applying the same bias potential of −4.0 V (versus Ag/AgCl) for 5 min, and X-ray diffraction measurements were carried out after the latter treatment.

Neutron reflectivity measurements and heavy water studies. Neutron reflectometry was performed at the Center for Neutron Research of the National Institute of Standards and Technology using the MAGIK reflectometer[29] in air with procedures similar to those described in ref. 30. The samples were characterized in the neutron beam over the Q range 0–0.18 $Å^{-1}$. The neutron reflectivity data were fitted with the NIST Refl1d software package (http://www.ncnr.nist.gov/reflpak). For the isotope substitution measurement, a SNO sample with thickness of about 70 nm was grown on a Si (100) substrate. The sample was cleaved into two pieces. The one piece was first characterized at the pristine state as a reference and was then treated at −4.0 V (versus Ag/AgCl) for 30 s in a 0.01 M KOH/H_2O solution. To observe the contrast from isotope substitution, the other piece of SNO was treated at −4.0 V (versus Ag/AgCl) for 30 s in a 0.01 M KOH/D_2O solution. After treatment, the samples were cleaned in isopropanol and dried in ambient conditions before the measurements.

Certain commercial equipment, instruments or materials are identified in this paper to foster understanding. Such identification does not imply recommendation or endorsement by the National Institute of Standards and Technology, nor does it imply that the materials or equipment mentioned are necessarily the best available for the purpose.

X-ray absorption spectroscopy. The XAS were measured at beamline 10ID-2 (REIXS) of the Canadian Light Source. The absorption near the Ni L_3 and O K edges was determined from the total fluorescence yield obtained with linearly polarized photons. The samples were placed in normal-incidence geometry with the electric field vector parallel to the (110) direction in a pseudocubic coordinate system. All spectra were measured at 20 K. For the X-ray absorption measurements, SNO samples with thickness of 70 nm were grown epitaxially on $LaAlO_3$ (001) substrates. Treatment was carried out in a 0.01 M KOH aqueous solution under a bias potential of −4.0 V (versus Ag/AgCl) for 30 s. After the treatment, the samples were rinsed with deionized water and dried with argon gas.

Optical spectra measurements. Reflection optical spectra in the near- and mid-infrared were measured using a Fourier transform infrared spectrometer and a mid-infrared microscope. For spectroscopic measurements of the transmission spectra, the samples were mounted in front of the opening of a gold integrating sphere, which captured both the direct and the diffused transmission of the samples. The signal was measured by a mercury cadmium telluride detector attached to the integrating sphere. The optical refractive indices were calculated by transfer matrix formalism (Supplementary Information section 6). To take an infrared image, a tunable mid-infrared quantum-cascade laser was used as the light source and irradiated the sample at a wavelength of 8 μm. For optical spectra measurements, SNO samples with thickness of 70 nm were grown on Si (100) substrates. The optical properties of Si substrates are well known, enabling us to quantitatively analyse the optical properties of SNO grown on Si. For infrared imaging, SNO samples with a thickness of 70 nm were grown on $LaAlO_3$ (001) substrates. Treatment was carried out in a 0.01 M KOH aqueous solution under a bias potential of −4.0 V (versus Ag/AgCl) for 30 s.

AIMD simulations of $SmNiO_3$–water interactions. AIMD simulations were performed with the Argonne Leadership Computing Facility supercomputers (2048 cores) using the generalized gradient approximation (GGA). The Hubbard correction to treat electron localization for Ni atoms used the projector-augmented wave formalism, as implemented in the Vienna Ab initio Simulation Package (VASP)[31,32]. The computational supercell consisted of a monoclinic SNO slab (160 atoms) with the surface normal pointing along the orthorhombic

crystallographic direction [110]. Periodic boundary conditions were employed along all directions with a vacuum of about 10 Å along the surface normal. For the SNO/water simulations, this vacuum was filled with 18 water molecules to simulate the experimental water density (1 g cm^{-3}). The exchange correlation was described by the Perdew–Burke–Ernzerhof functional[33], with the pseudopotentials Sm_3 (valence $5s^2\ 5p^2\ 6s^2\ 4f^1$), Ni_pv (valence $3p^6\ 4s^2\ 3d^8$) and O (valence $2s^2\ 2p^4$) supplied by VASP. The plane-wave energy cut-off was set at 520 eV. The Brillouin zone was sampled at the Γ-point only. Using AIMD simulations in the isobaric-isothermal ensemble, we first thermalized the SNO (110) computational supercell at various temperatures ranging from 300 K to 500 K and zero external pressure for 10 ps using a time step of 0.5 fs. During these simulations, the cell volume, cell shape and atomic positions were allowed to vary via the Parrinello–Rahman scheme[34]. The temperature conditions were maintained by using a Langevin thermostat. Next, we inserted the water molecules in the vacuum (at a given temperature). The subsequent AIMD simulations were performed in the canonical ensemble (constant volume and temperature). Constant temperature conditions were maintained via a Nosé–Hoover thermostat[35], as implemented in VASP. To identify the activation barriers and minimum energy paths for H intercalation into a SNO (110) slab, we employed the climbing image nudged elastic band method within the GGA + U formalism[36], where U is the on-site Coulomb parameter. The diffusion coefficient (D) of protons in bulk SNO at 300 K was estimated using the Einstein relationship $D = [r(t) - r(0)]^2/(6t)$, where $[r(t) - r(0)]^2$ is the mean-square displacement of a proton at time t with respect to the time origin ($t = 0$); the value of D was averaged over various time domains (each of duration 0.5 ps) over the AIMD trajectory.

First-principles electronic structure calculations of HSNO. First-principles calculations were carried out within the DFT + U approximation with the VASP code[31,32] using the projector augmented plane-wave method of DFT[37] and the pseudopotentials Sm_3 (valence $5s^2\ 5p2\ 6s^2\ 4f^1$), Ni_pv (valence $3p6\ 4s^2\ 3d^8$), O (valence $2s^2\ 2p^4$) and H (valence $1s^1$).To treat the exchange and correlation, the Perdew–Burke–Ernzerhof functional was used within the GGA[33] and the rotationally invariant form of DFT + U of ref. 34 with $U = 4.6$ eV and $J = 0.6$ eV, where J is the on-site exchange parameter. For the structural determination of pristine SNO, we started with the Materials Project structure[38], added a small monoclinic distortion ($\beta \approx 90.75$) and allowed the cell and ionic positions to relax until the forces on each ion were lower than 0.005 eV $Å^{-1}$. All calculations were carried out with the tetrahedral method with Blöchl corrections[39], a $6 \times 6 \times 4$ Monkhorst–Pack k-point mesh for the $\sqrt{2} \times \sqrt{2} \times 2$ supercell, and a plane-wave energy cut-off of 500 eV. To determine the structure of HSNO, we began with $H_{0.25}SmNiO_3$, adding one hydrogen atom at various locations to the pristine SNO $\sqrt{2} \times \sqrt{2} \times 2$ supercell with G-type magnetic ordering, and allowed the internal coordinates to relax with the same tolerance as described above. The structure with the lowest energy was chosen as the $H_{0.25}SmNiO_3$ structure. Taking the symmetry-equivalent site of the relaxed hydrogen position, we constructed structures for $H_{0.5-1}SmNiO_3$, again allowing the internal coordinates to relax (Supplementary Information section 7). We compared the results while keeping the total volume of the cell fixed and relaxing the volume and the [110] direction only, where the qualitative features of the electronic structure were not affected.

Data availability. The data that support the findings of this study are available from the corresponding author upon reasonable request.

29. Dura, J. A. *et al.* AND/R: advanced neutron diffractometer/reflectometer for investigation of thin films and multilayers for the life sciences. *Rev. Sci. Instrum.* **77,** 74301 (2006).
30. DeCaluwe, S. C., Kienzle, P. A., Bhargava, P., Baker, A. M. & Dura, J. A. Phase segregation of sulfonate groups in Nafion interface lamellae, quantified via neutron reflectometry fitting techniques for multi-layered structures. *Soft Matter* **10,** 5763–5776 (2014).
31. Kresse, G. & Furthmüller, J. Efficient iterative schemes for *ab initio* total-energy calculations using a plane-wave basis set. *Phys. Rev. B* **54,** 11169–11186 (1996).
32. Kresse, G. & Joubert, D. From ultrasoft pseudopotentials to the projector augmented-wave method. *Phys. Rev. B* **59,** 1758–1775 (1999).
33. Perdew, J. P., Burke, K. & Ernzerhof, M. Generalized gradient approximation made simple. *Phys. Rev. Lett.* **77,** 3865–3868 (1996).
34. Liechtenstein, A. I., Anisimov, V. I. & Zaanen, J. Density-functional theory and strong interactions: orbital ordering in Mott-Hubbard insulators. *Phys. Rev. B* **52,** R5467 (1995).
35. Allen, M. P. & Tildesley, D. J. *Computer Simulation of Liquids* (Oxford Univ. Press, 1989).
36. Henkelman, G., Uberuaga, B. P. & Jónsson, H. A climbing image nudged elastic band method for finding saddle points and minimum energy paths. *J. Chem. Phys.* **113,** 9901–9904 (2000).
37. Blöchl, P. E. Projector augmented-wave method. *Phys. Rev. B* **50,** 17953–17979 (1994).
38. Persson, K. *Materials Data on $SmNiO_3$ (SG:62) by Materials Project.* Dataset No. mp-25588 (Lawrence Berkeley National Laboratory, 2016); https://materialsproject.org/materials/mp-25588/.
39. Blöchl, P. E., Jepsen, O. & Andersen, O. K. Improved tetrahedron method for Brillouin-zone integrations. *Phys. Rev. B* **49,** 16223–16233 (1994).
40. Pérez-Cacho, J., Blasco, J., Garcia, J., Castro, M. & Stankiewicz, J. Study of the phase transitions in $SmNiO_3$. *J. Phys. Condens. Matter* **11,** 405–415 (1999).
41. Shi, J., Ha, S. D., Zhou, Y., Schoofs, F. & Ramanathan, S. A correlated nickelate synaptic transistor. *Nat. Commun.* **4,** 2676 (2013).
42. Wootton, J. T., Pfister, C. A. & Forester, J. D. Dynamic patterns and ecological impacts of declining ocean pH in a high-resolution multi-year dataset. *Proc. Natl Acad. Sci. USA* **105,** 18848–18853 (2008).
43. Mamayev, O. I. *Temperature–Salinity Analysis of World Ocean Waters* Vol. 11, 305–334 (Elsevier, 1975).

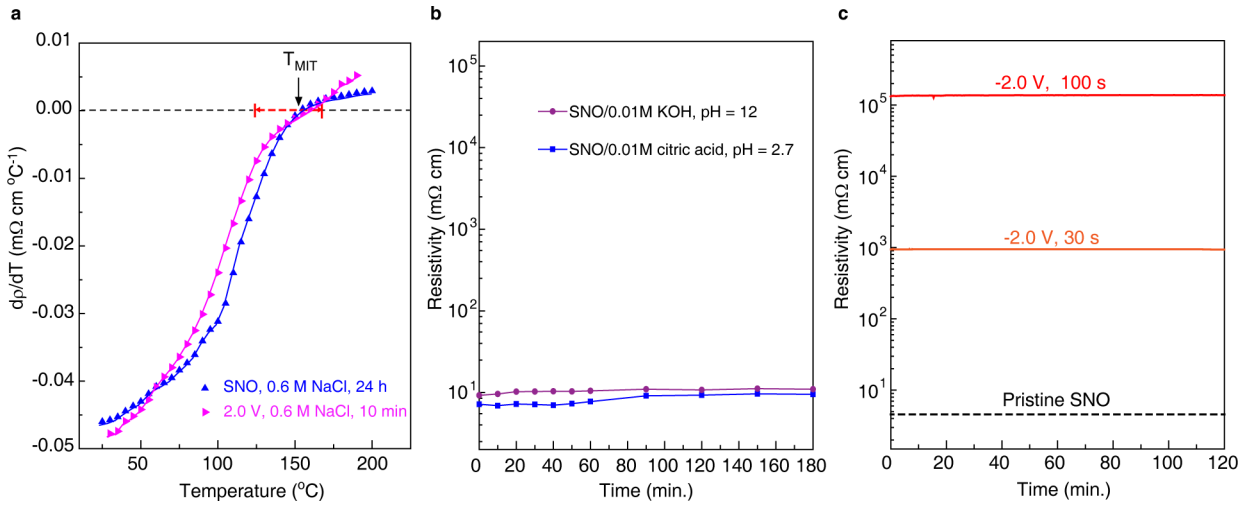

Extended Data Figure 1 | Electrical properties of water-treated SNO. a, Temperature derivative of the electrical resistivity of SNO after submersion in a 0.6 M NaCl aqueous solution for 24 h (blue curve). The insulator–metal transition temperature (T_{MIT}), where $d\rho/dT$ changes sign from negative to positive for submerged SNO is in the same range as reported in the literature[5,7,40,41]. The purple curve shows the temperature derivative of the electrical resistivity of SNO obtained after applying a reverse bias of 2.0 V for 10 min to a water-treated HSNO sample, where the metal–insulator transition recovers. **b**, Electrical resistivity of SNO after being submerged in solutions of 0.01 M KOH and 0.01 M citric acid. The electrical resistivity of SNO shows minimal variation over a wide range of pH values for 180 min. **c**, Non-volatile behaviour of SNO thin film after applying a bias of −2.0 V in a 0.6 M NaCl solution for various durations. The resistivity of SNO after sensing an electric potential remains unchanged for 120 min, which demonstrates its non-volatile nature, in contrast to the surface electrostatic field effect of electric double-layer transistors.

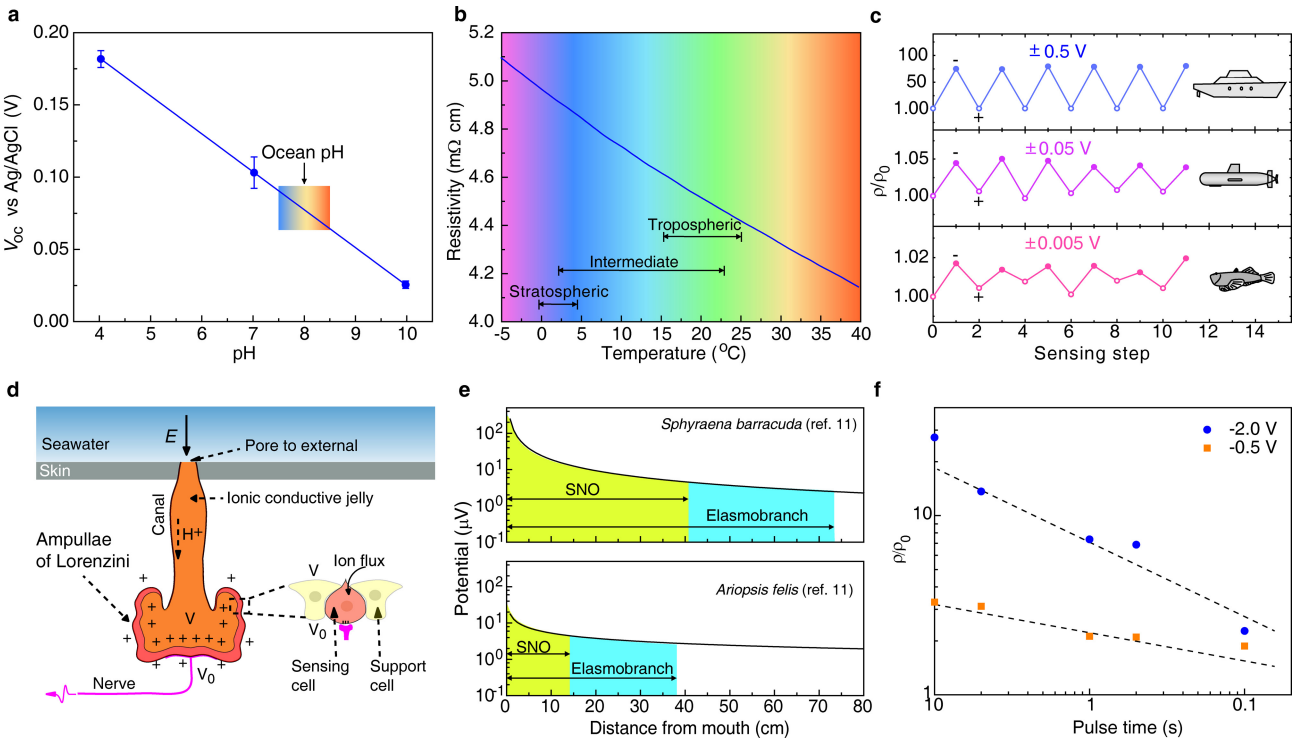

Extended Data Figure 2 | pH, temperature and electric potential sensing of SNO. a, Open-circuit potential (V_{OC}) of SNO relative to a standard Ag/AgCl electrode in standard aqueous buffers with pH values covering the pH range of Earth's oceans[42]. Error bars show the standard deviation. The potential V_{OC} decreases monotonically with increasing pH. This linear relationship between proton activity (and the corresponding surface adsorption) and V_{OC} enables SNO to operate as a pH sensor. **b**, Temperature-dependent electrical resistivity of SNO in the temperature range of Earth's oceans[43]. The electrical resistivity increases with cooling; this is consistent with the insulating nature of SNO around room temperature, which enables it to function as a thermistor. **c**, Modulation of normalized electrical resistivity of SNO in an aqueous environment after the application of bias potentials over multiple sensing steps. The bias potentials (versus Ag/AgCl) were ±0.5 V, ±0.05 V and ±0.005 V and their duration was 10 s. The aqueous environment was a 0.6 M NaCl solution with salinity close to that of sea water. The normalized resistivity increases and then decreases following the reversal of the bias potential. The reversibility of the water-mediated phase transition and the facile migration of protons enable SNO to detect the local fluctuation of electric signals in water. This sensing capability persists over multiple cycles, indicating their robustness in aqueous environments. **d**, Schematic of an ampulla of Lorenzini, an electroreception organ located around the mouth of sharks. **e**, Electric potential as a function of distance for teleost fishes (*Sphyraena barracuda* and *Ariopsis felis*)[11]. The detection range of elasmobranch predators[11] and SNO sensors are shaded with blue and yellow colour, respectively. The calculated detection range of SNO includes the regime where the bioelectric potential of prey fishes is higher than the sensitivity of SNO (about 4.5 μV) experimentally determined from Fig. 1g. The nickelate device is estimated to detect field stimuli over a distance of tens of centimetres, which is similar in range to that of elasmobranch species. **f**, Experimentally measured resistance modulation of pristine SNO upon the application of pulsed bias potential at −2.0 V and −0.5 V respectively. The response times of the SNO sensor studied here are as low as 0.1 s.

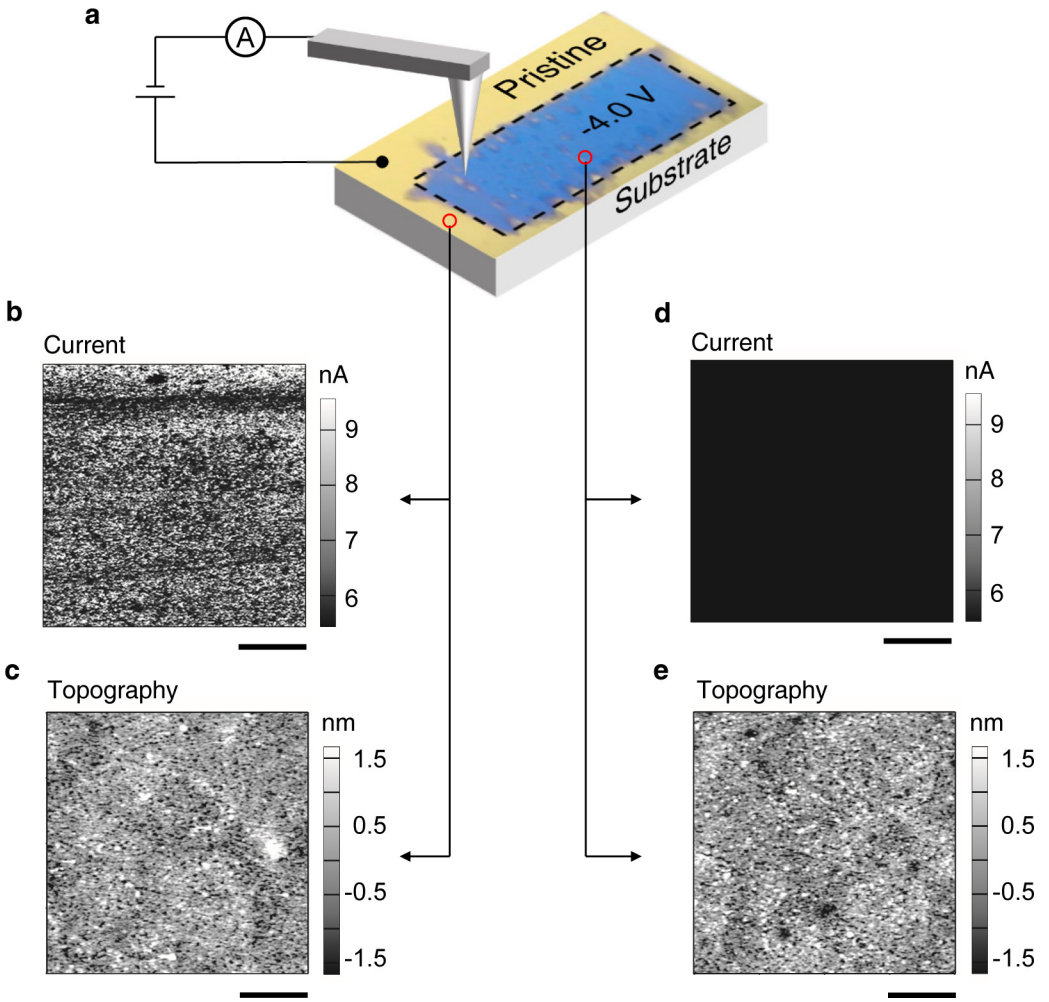

Extended Data Figure 3 | Topography and current map of water-treated SNO thin films. a, Optical image of SNO after applying bias to a selected area, where colour change occurs. **b**, Current map of pristine area, where the current is in the nanoampere range. **c**, The corresponding surface topography of the pristine area. **d**, Current map of water-treated area, which is entirely dark compared with the pristine state (**b**). The current after sensing is decreased to the picoampere range owing to proton uptake. **e**, The corresponding surface topography of SNO after sensing, where no evidence of corrosion was observed compared with the pristine state (**c**). Moreover, almost no variance is observed in the surface roughness of the thin film (Supplementary Information section 3). Scale bars are 0.5 μm.

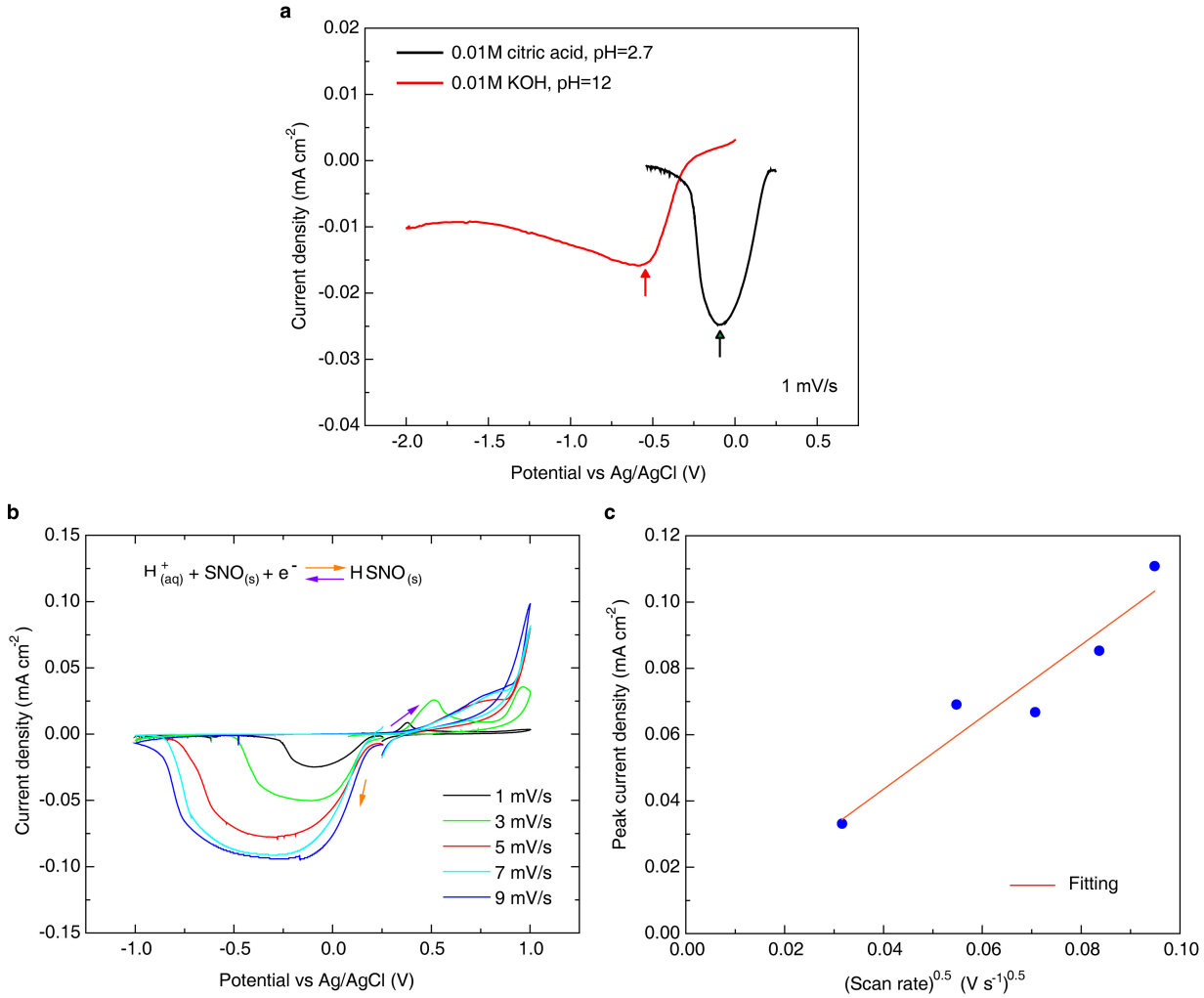

Extended Data Figure 4 | Cyclic voltammograms of SNO thin films. **a**, Dependence of water-mediated phase transition in SNO on pH values spanning from an acidic solution (0.01 M citric acid, pH = 2.7) to a basic solution (0.01 M KOH, pH = 12). The transition from SNO to HSNO shifts to more negative potential values with increasing pH, where greater bias is required to compensate for the reduction of the proton activity in the basic solutions. **b**, Cyclic voltammogram and accompanying reaction for SNO in 0.01 M citric acid from 1.0 V to −1.0 V (versus Ag/AgCl) at various scan rates. Cathodic current peaks at negative potentials indicate the charge transfer as the Ni^{3+} is reduced to Ni^{2+}. The peak position varies as a function of scan rate, indicating that the reaction is kinetically limited by the charge and mass transfer. **c**, Linear relationship between peak cathodic current density (I_p/A) and the square root of the scan rate ($\nu^{0.5}$). The best fit to the Randles–Sevcik equation[23] estimates the number of electrons transferred in the rate-limiting step as 0.95 (Supplementary Information section 4), indicating that the Ni in SNO is almost fully reduced from Ni^{3+} to Ni^{2+} upon intercalation.

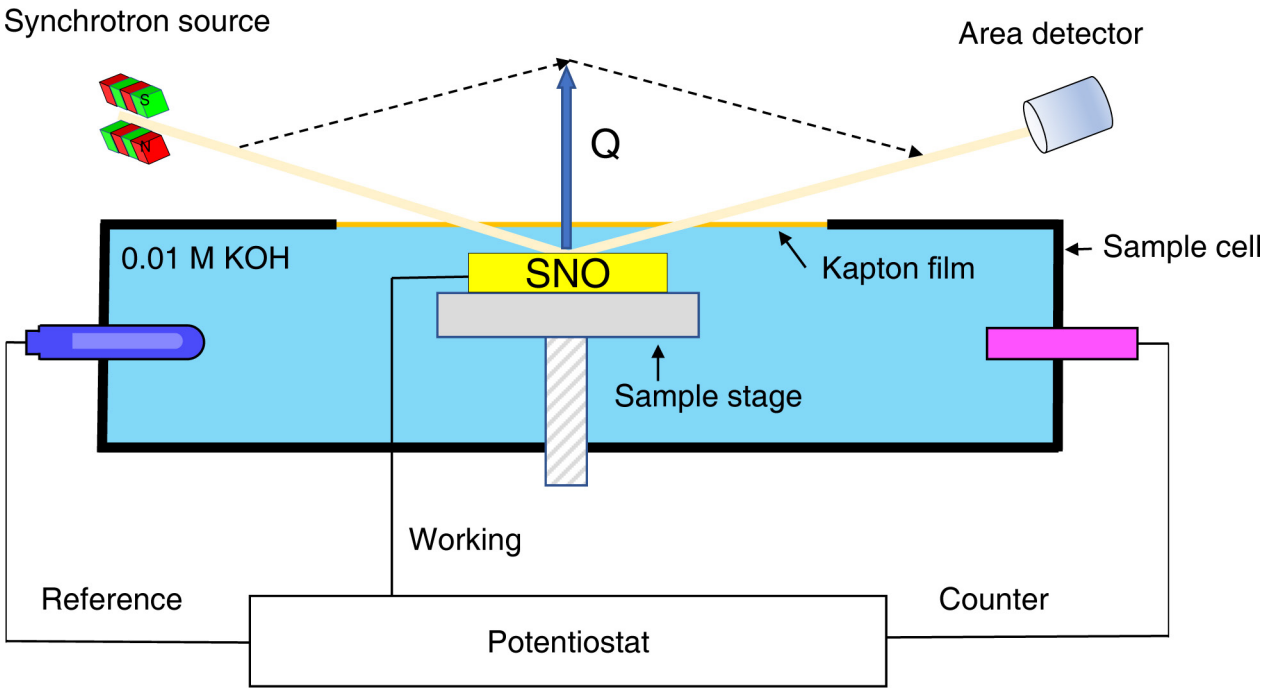

Extended Data Figure 5 | A schematic of the experimental setup for *in situ* XRR measurement at the Advanced Photon Source. The SNO thin film was connected to a working electrode and submerged in a 0.01 M KOH aqueous solution. A Kapton film was used to avoid the spillage of electrolyte during measurement. The electric potential was applied through the counter-electrode. After the treatment, the XRR signals were collected *in situ*.

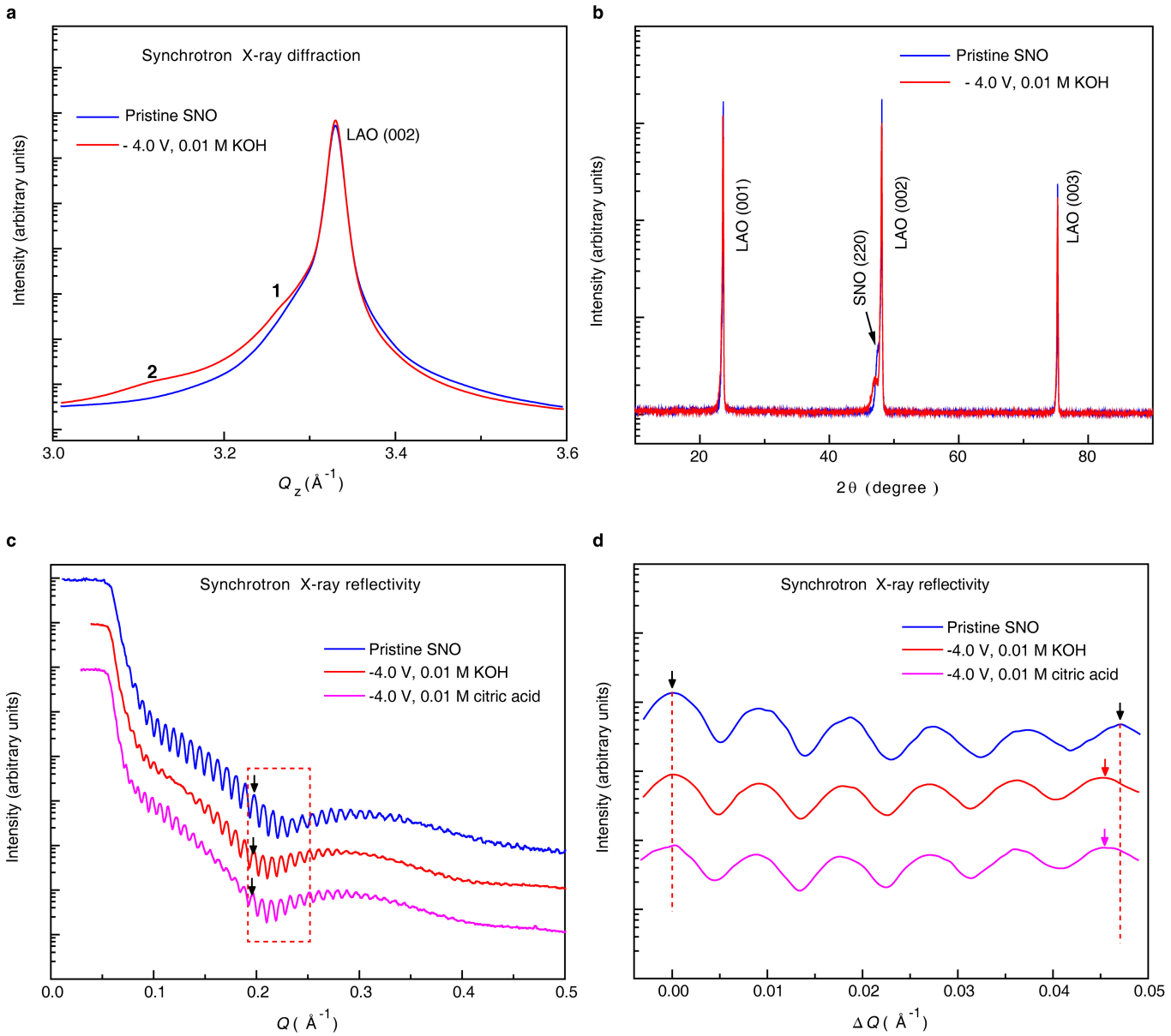

Extended Data Figure 6 | X-ray diffraction and X-ray reflectivity of water-treated SNO. a, Synchrotron X-ray diffraction curves taken from a SNO/$LaAlO_3$ thin film after treatment in a 0.01 M KOH aqueous solution at −4.0 V for 30 s. The (220) peak of pristine SNO (orthorhombic notation) appears at $Q_1 \approx 3.29$ Å^{-1} as a shoulder with slightly lower scattering vector Q_z than the $LaAlO_3$ (002) diffraction peak (pseudocubic notation), demonstrating the epitaxial growth of SNO on $LaAlO_3$. After the water treatment, the epitaxial relationship of SNO on $LaAlO_3$ is preserved. Peak 1 shifts to a lower Q_z. Peak 2 appears at $Q_z = 3.11$ Å^{-1}, which corresponds to increase of the lattice constant by 5.7%. LAO stands for $LaAlO_3$. **b**, X-ray diffraction profiles of SNO and water-treated SNO over a wide range of scattering angles 2θ. No new peaks appear, in contrast to what has been observed in other oxides, such as cobaltites, upon exposure to water. **c**, Comparison of synchrotron XRR curves for SNO after applying a bias of −4.0 V for 5 min in 0.01 M citric acid and 0.01 M KOH aqueous solutions. **d**, A selected area of the XRR curves, normalized to the oscillation peak at $Q \approx 0.19$ Å^{-1} (marked by black arrows in **c**). Upon treatment, the XRR oscillation period decreases, demonstrating film expansion regardless of solution type, which indicates a general mechanism of phase change of SNO in various aqueous solutions caused by proton incorporation.

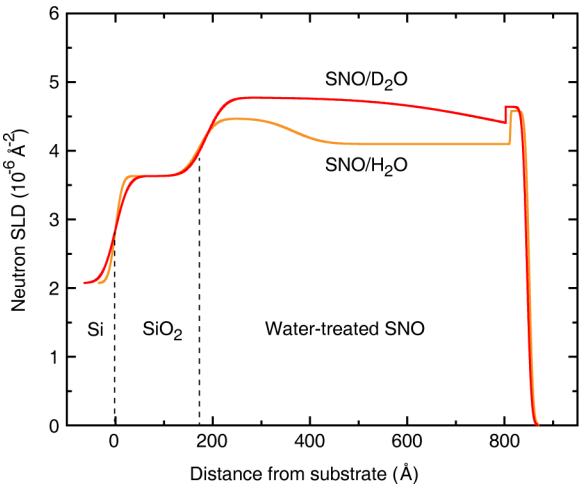

Extended Data Figure 7 | Neutron scattering length density profiles of heavy-water-treated SNO. The scattering length density (SLD) profiles were fitted to the data shown in Fig. 2b for the SNO/SiO_2/Si films. The surface roughness is nearly unchanged after water treatment (Supplementary Information section 3). The profiles of water-treated and heavy-water-treated samples show similar film expansion. However, differences exist between the scattering length densities of D_2O- and H_2O-treated films. Because D^+ has larger neutron scattering length than H^+, the increase of the scattering length density demonstrates the intercalation of D^+ from D_2O into the lattice after the treatment.

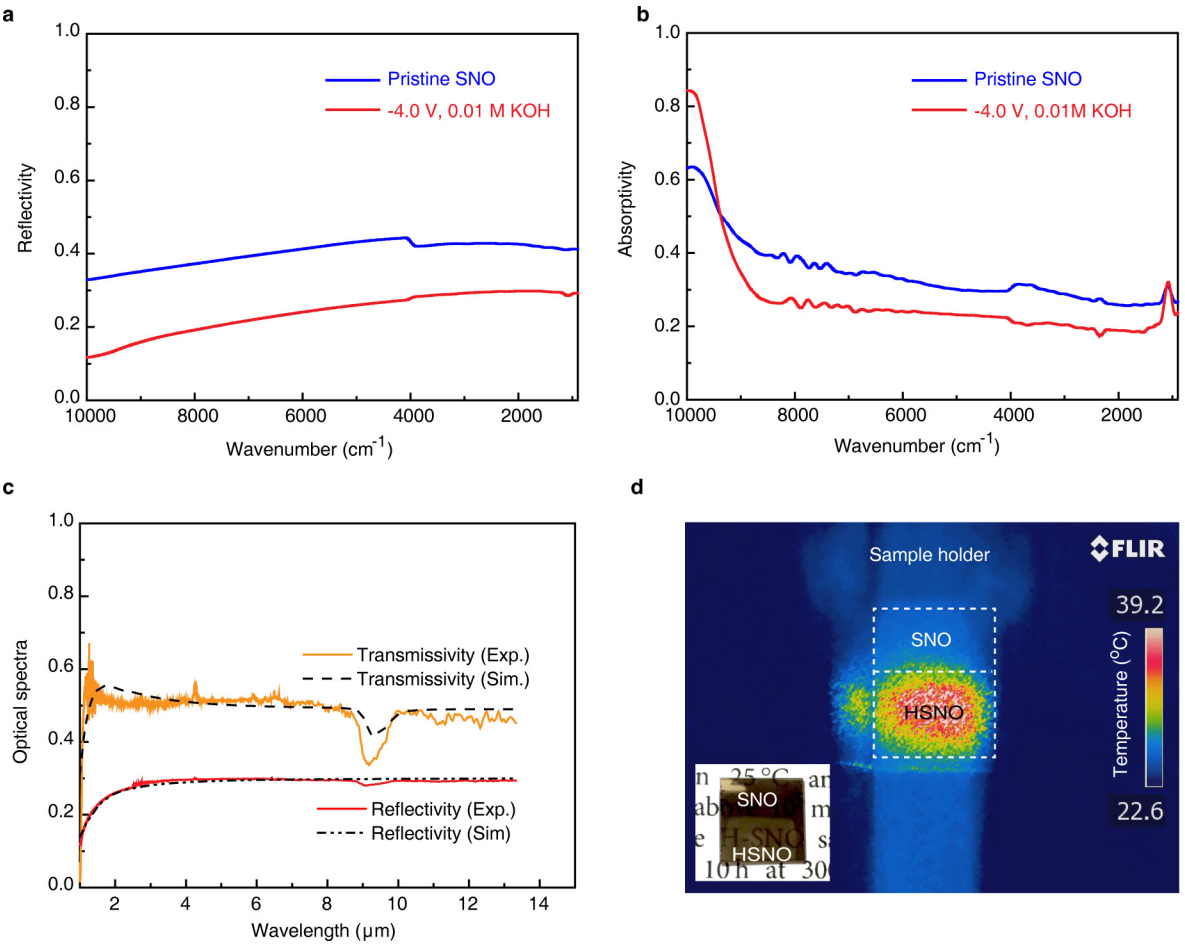

Extended Data Figure 8 | Optical spectra of water-treated SNO. **a**, **b**, Reflectivity (**a**) and absorptivity (**b**) of pristine and water-treated (−4.0 V, 30 s, in 0.01 M KOH aqueous solution) SNO thin film deposited on a Si substrate. After the treatment, the SNO sensing device shows reduction in both reflectivity and free-electron absorptivity, concurrent with a large increase in electrical resistance. **c**, Finite-difference time-domain simulation of optical spectra of water-treated SNO/SiO_2/Si thin film devices. The experimental results of the transmissivity and reflectivity of water-treated SNO are compared with finite-difference time-domain simulation results of HSNO/SiO_2/Si thin film devices, where the optical parameters of samples treated with gas-phase hydrogen[27] were adopted for HSNO. The good agreement between experimental and simulation results indicates the occurrence of a phase transition from SNO to HSNO during water treatment with no material decomposition. The thickness of SNO and SiO_2 was obtained from neutron reflectivity data. The SiO_2 layer between the SNO thin film and Si, which is formed during film synthesis, contributes to the absorption feature observed at 9.2 μm in the transmission spectra. **d**, An infrared image of a SNO/$LaAlO_3$ sample with water treatment on a selected area (FLIR, infrared camera). SNO becomes more transparent (red colour) in the infrared wavelength range at $\lambda = 8$ μm after the treatment. The inset shows a photograph of the sample, where the transparency of the treated area can be observed in the visible wavelength range.

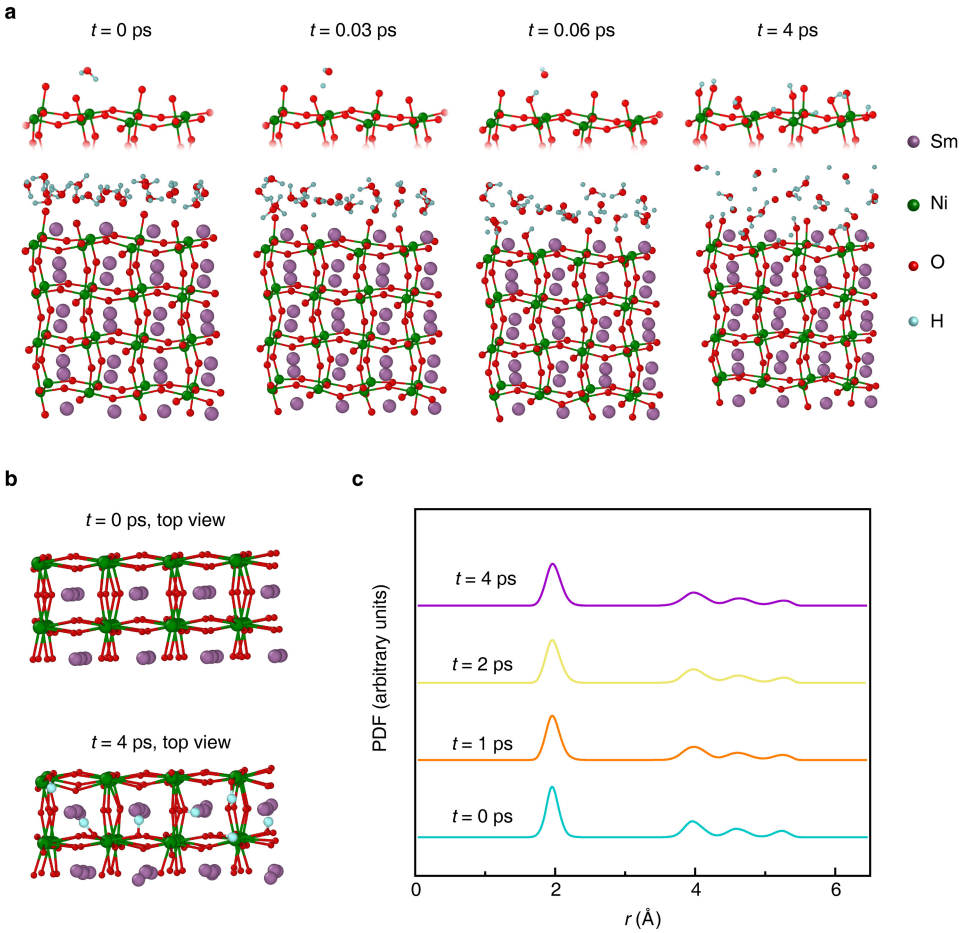

Extended Data Figure 9 | Dynamic simulations of SNO–water interactions at an elevated temperature of 500 K. a, Snapshots of the temporal evolution of a SNO surface submerged in water. Images tracking the evolution of a typical water molecule and the NiO_6 octahedra in the SNO layer closest to water are shown in the top panels. At 500 K, the surface protonation mechanisms are identical to those at ambient temperature, where water at the SNO surface dissociates into free protons and OH^-; a fraction of the free protons migrates to the oxide/water interface and binds to the surface oxygen of SNO. These atomic-scale processes observed in AIMD simulations support the proton accumulation and surface protonation mechanism depicted schematically in Fig. 1a. **b**, Top view, showing SNO protonation at the end of 4 ps. Compared with the pristine state at 0 ps, the SNO surface maintains structural stability during the protonation, even at 500 K (well above ocean temperature). **c**, The Ni–O pair distribution functions (PDF) calculated at various time intervals. The curves demonstrate well defined sharp peaks, suggesting that the SNO surface remains intact after surface protonation at elevated temperature in an aqueous environment. These results are consistent with the good stability inferred from the temperature-dependent electrical resistivity measurement of the submerged SNO samples.

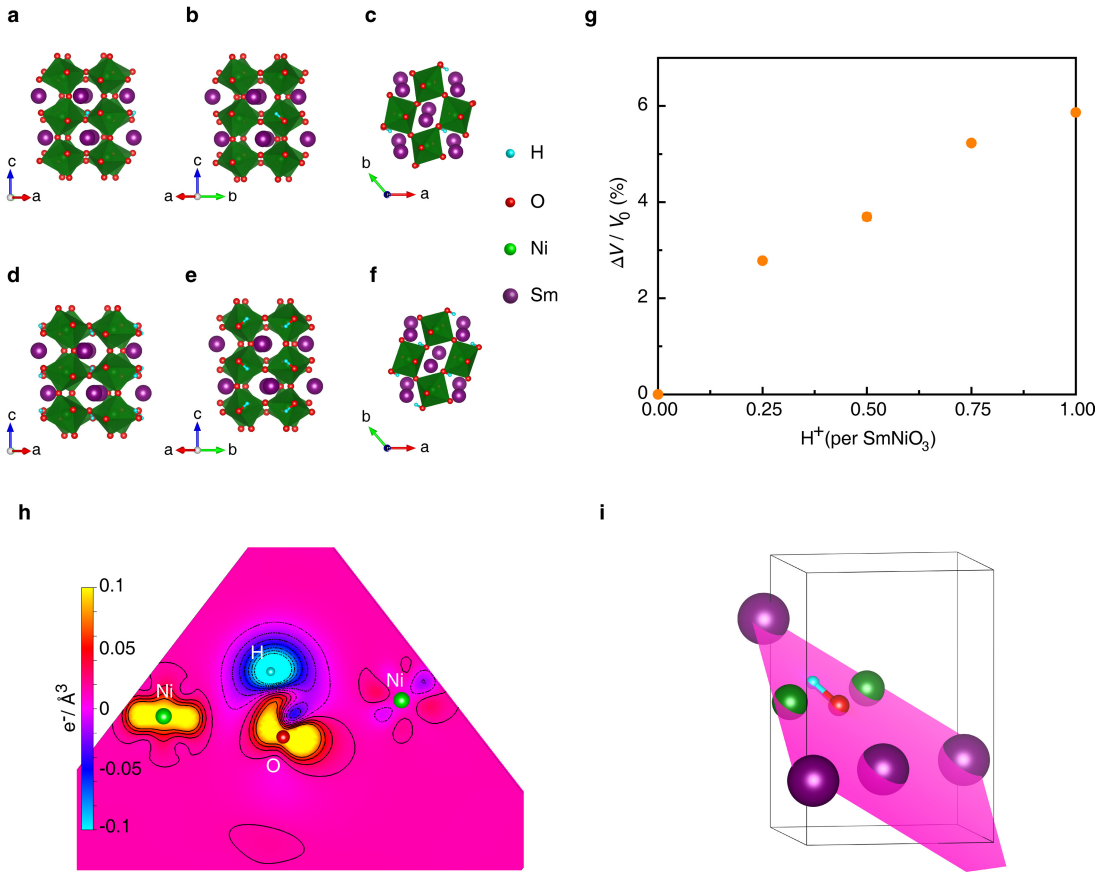

Extended Data Figure 10 | First-principles calculations of the structure and electron localization of HSNO. a–f, The structure of SNO with 1/4 H/SNO (**a–c**) and 1 H/SNO (**d–f**), displayed along the three crystallographic axes of the primitive perovskite structure. The crystallographic axes of the supercell were used in the calculations, where the [110] direction was allowed to relax. In all panels, 12 NiO_6 octahedra encompassing the Ni atoms (green) are displayed, with O in red, Sm in purple and H in cyan. The calculations use a $\sqrt{2} \times \sqrt{2} \times 2$ supercell (that is, with four Ni atoms). **g**, Change in the volume of SNO at various protonation levels (denoted as protons per SNO formula unit) obtained from DFT calculations. The calculated volume expansion for 1 H/SNO is about 5.9%, which is close to the value obtained from neutron reflectometry measurements and X-ray diffraction. **h**, The difference in the electron density between the relaxed HSNO ($SmNiO_3H$) and the initial state (SNO + H), which clearly shows a depletion (cyan) of charge around the hydrogen (cyan) and an accumulation (yellow) of charge around the closest nickel (green) and oxygen (red), which are part of the octahedron that expands upon hydrogen incorporation into the lattice. In this calculation, the *c* axis was allowed to relax while the other two (in-plane lattice constants) were fixed. For clarity, only the spin-down charge density is plotted because the electron incorporation results in a negative total magnetic moment (see the projected density of states of 1/4 H/SNO in Fig. 3d). **i**, The $(\bar{1}11)$ plane of the contour plot situated within the supercell.